J|A|C|S
JOURNAL OF THE AMERICAN CHEMICAL SOCIETY

ARTICLE

pubs.acs.org/JACS

# High Performance Thermoelectrics from Earth-Abundant Materials: Enhanced Figure of Merit in PbS by Second Phase Nanostructures

Li-Dong Zhao,[†] Shih-Han Lo,[‡] Jiaqing He,[†,‡] Hao Li,[†] Kanishka Biswas,[†] John Androulakis,[†] Chun-I Wu,[§] Timothy P. Hogan,[§] Duck-Young Chung,[∥] Vinayak P. Dravid,[‡] and Mercouri G. Kanatzidis*[,†,∥]

[†]Department of Chemistry, and [‡]Department of Materials Science and Engineering, Northwestern University, Evanston, Illinois 60208, United States

[§]Department of Electrical and Computer Engineering, Michigan State University, East Lansing, Michigan 48824, United States

[∥]Materials Science Division, Argonne National Laboratory, Argonne, Illinois 60439, United States

S *Supporting Information*

**ABSTRACT:** Lead sulfide, a compound consisting of elements with high natural abundance, can be converted into an excellent thermoelectric material. We report extensive doping studies, which show that the power factor maximum for pure n-type PbS can be raised substantially to $\sim$12 $\mu$W cm$^{-1}$ K$^{-2}$ at >723 K using 1.0 mol % $PbCl_2$ as the electron donor dopant. We also report that the lattice thermal conductivity of PbS can be greatly reduced by adding selected metal sulfide phases. The thermal conductivity at 723 K can be reduced by $\sim$50%, 52%, 30%, and 42% through introduction of up to 5.0 mol % $Bi_2S_3$, $Sb_2S_3$, SrS, and CaS, respectively. These phases form as nanoscale precipitates in the PbS matrix, as confirmed by transmission electron microscopy (TEM), and the experimental results show that they cause huge phonon scattering. As a consequence of this nanostructuring, *ZT* values as high as 0.8 and 0.78 at 723 K can be obtained for nominal bulk PbS material. When processed with spark plasma sintering, PbS samples with 1.0 mol % $Bi_2S_3$ dispersion phase and doped with 1.0 mol % $PbCl_2$ show even lower levels of lattice thermal conductivity and further enhanced *ZT* values of 1.1 at 923 K. The promising thermoelectric properties promote PbS as a robust alternative to PbTe and other thermoelectric materials.

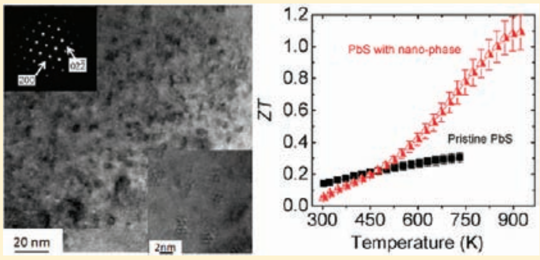

## INTRODUCTION

Thermoelectric materials, capable of creating electricity from waste heat sources, are attractive in the search for sustainable energy management and currently are receiving significant scientific attention.[1,2] The efficiency of thermoelectric devices is determined by the dimensionless figure of merit (*ZT*), defined as $ZT = (S^2\sigma/\kappa)T$, where $S$, $\sigma$, $\kappa$, and $T$ are the Seebeck coefficient, the electrical conductivity, the thermal conductivity, and the absolute temperature, respectively. Therefore, excellent thermoelectric materials require a perfect combination of high power factor ($S^2\sigma$) and low thermal conductivity ($\kappa$). To date, several classes of bulk materials with high *ZT* values have been discovered, including nanostructured BiSbTe alloys,[3] $AgPb_mSbTe_{m+2}$(LAST),[4] Tl doped PbTe,[5] $(AgSbTe_2)_{1-x}(GeTe)_x$,[6] Na doped $PbTe_{1-x}Se_x$,[7] $AgPb_mSn_nSbTe_{m+n+2}$(LASTT),[8] $NaPb_mSbTe_{m+2}$(SALT),[9] PbTe−PbS,[10] PbTe−SrTe,[11] and K/Na codoped PbTe.[12] These materials show high performance at room and middle temperature range (600−850 K); however, the common feature of these materials is that they contain a significant amount of Te, which is a scarce element in the crust of the earth. Hence, the Te price is likely to rise sharply if Te-based thermoelectric materials reach mass markets. A broad search for more inexpensive alternatives is therefore warranted.[13−16]

PbS could potentially be such a high alternative because it has many attractive features. For example, PbS shares the same highly symmetric NaCl−type cubic structure as its heavier congeners, it is composed of abundant elements, and it has an even higher melting point (1391 K) and energy band gap (0.41 eV). By comparison, PbTe has 1197 K and 0.32 eV, respectively. Previous work in the literature performed decades ago indicated that PbS was not an attractive thermoelectric material with a maximum $ZT \approx 0.4$ at 800 K, and it was subsequently neglected in favor of PbTe.[17−20] Recently, we investigated the thermoelectric properties of compositions lying in the PbS-rich side of the PbS−PbTe phase diagram and reported that significant thermoelectric enhancements can be achieved.[16] These results imply that PbS-based materials may in fact be promising for high temperature application with continued improvements. This motivated us to expand our investigations of PbS to completely Te-free systems and bring to bear many of the new concepts and ideas developed for PbTe itself, which have been so successful in producing record-breaking performances.[5−12]

Usually, reducing the thermal conductivity is an effective way to enhance *ZT*, and it can be reduced significantly by introducing grain boundaries or interfaces, for example, nanocrystalline inclusions.[3] Two important points need to be made here; first, not all nanocrystalline inclusions are effective,[21,22] and, second, the

**Received:** September 14, 2011
**Published:** November 29, 2011

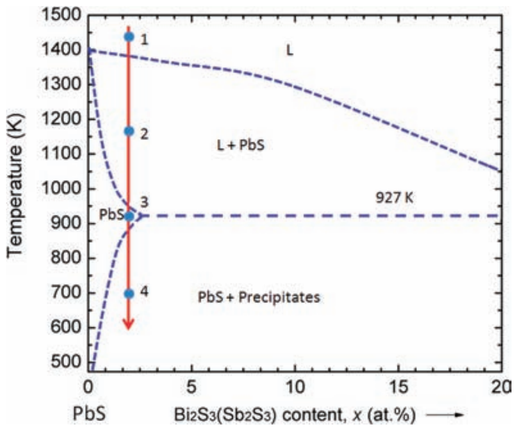

**Figure 1.** Binary phase diagram of PbS–$Bi_2S_3$($Sb_2S_3$), adapted from ref 30, indicating a strongly temperature-dependent solubility of $Bi_2S_3$ ($Sb_2S_3$) in PbS.

suppression of lattice thermal conductivity ($\kappa_L$) is generally overshadowed by the deterioration of carrier mobility ($\mu$). Apart from the grain boundary scattering, obvious $ZT$ improvements have been reported by adding nano-SiC particles in $Bi_2Te_3$,[23] dispersing in situ partially oxidized $Yb_2O_3$ nanoparticles in $CoSb_3$.[24] It is also reported that more significant enhancements can be achieved by embedding metal or conductive nanoparticles into a thermoelectric material matrix: examples include Pb and Sb in PbTe,[25] Sb in $YbCoSb_{12}$,[26] and ErAs in $In_{0.53}Ga_{0.47}As$.[27] A well-known example of thermal conductivity reduction in PbTe-based materials is $AgPb_mSbTe_{2+m}$ (LAST, considered as PbTe alloyed with $AgSbTe_2$ or codoped with Ag and Sb) and other related systems,[8,9,28] where endotaxial nanometer-sized inclusions are thought to play a key role in scattering phonons while not affecting electrons.

In this Article, we focus on PbS, a very stable and simple material, which contains highly abundant elements. In this system, we targeted the reduction of thermal conductivity using the nanostructuring technique. A general approach for introducing nanostructures in the PbS matrix is the nucleation and growth technique,[10,29] which can be described as follows: we choose the second phase candidates to have very low or no solubility in the solid state, but complete solubility in the liquid state. The second phase will be precipitated because it reaches or exceeds the solid state solution limit if the melt is quenched by rapid cooling. The technique used here for the formation of precipitates is elaborated in Figure 1. The estimated section of the pseudobinary phase diagram for the PbS–$Bi_2S_3$ ($Sb_2S_3$) system is adapted from ref 30, and it suggests a strongly temperature-dependent solubility of $Bi_2S_3$ ($Sb_2S_3$) in PbS. The mixture of PbS and $Bi_2S_3$ ($Sb_2S_3$) gives a homogeneous melt above 1391 K (step 1), which then is cooled in step 2, and after that the sample is quenched and annealed within the single phase region (at this stage, the $Bi_2S_3$ or $Sb_2S_3$ dissolve in the PbS matrix). In step 3, phase separation and precipitation of the second phases is achieved by cooling after reaching the solid state solubility limit curve in step 4. For these samples, we chose $PbCl_2$ as the electron donor dopant to tune the carrier concentration through substituting $S^{2-}$ by $Cl^-$ to optimize the power factor. Here, we show that these nanoscale phases of $Bi_2S_3$ and $Sb_2S_3$ (as well as CaS and SrS) greatly reduce the thermal conductivity of PbS to levels similar to those achieved in nanostructured PbTe. As a result, we have obtained the $ZT$ value of 1.1 at 923 K for n-type PbS samples nanostructured with 1.0 mol % $Bi_2S_3$ and doped with 1.0 mol % $PbCl_2$, which is the highest ever reported for this system.

## ■ EXPERIMENTAL SECTION

**Synthesis.** Reagents chemicals were used as obtained: Pb wire (99.99%, American Elements, U.S.), S shot or chunk (99.999%, Inc., Canada), Bi chunk (99.999%, Noranda, Canada), Sb shot form (99.999%, Noranda, Canada), Sr chunk (99.9%, Cerac, U.S.), Ca redistilled granule (99.5%, Alfa Aesar, U.S.), and $PbCl_2$ powders (99.999%, Aldrich, U.S.).

Starting powders, such as PbS, $Bi_2S_3$, $Sb_2S_3$, and SrS, were prepared first. PbS was prepared by a melting reaction method using mixing elemental Pb and S inside carbon-coated fused silica tubes; the tubes were then evacuated to a base pressure of $\sim 10^{-4}$ Torr, flame-sealed, slowly heated to 723 K in 12 h, then heated to 1423 K in 7 h, soaked at this temperature for 6 h, and subsequently air quenched to room temperature. $Bi_2S_3$ was prepared by mixing elemental Bi and S inside fused silica tubes. The tubes were subsequently evacuated to a base pressure of $\sim 10^{-4}$ Torr, fused, slowly heated to 723 K in 12 h, then heated to 1223 K in 5 h, soaked at this temperature for 6 h, and subsequently cooled to room temperature. The synthesis procedure for $Sb_2S_3$ was the same as that of $Bi_2S_3$. SrS was synthesized using elemental Sr and S inside an $Al_2O_3$ crucible and then charged in a fused silica tube. The manipulations and preparative steps for the SrS starting powders were carried out within a purified Ar-atmosphere glovebox, with total $O_2$ and $H_2O$ level <0.1 ppm. The silica tubes were subsequently evacuated to a base pressure of $\sim 10^{-4}$ Torr, fused, slowly heated to 723 K in 12 h, then heated to 1153 K in 4 h, soaked at this temperature for 20 h, and subsequently cooled to room temperature. PbS ingots ($\sim$10 g) with $x$ mol % doping $PbCl_2$ ($x$ = 0, 0.04, 0.80, 1.0, 2.0, and 5.0) and/or with $y$ mol % ($y$ = 0, 1.0, 2.0, 3.0, 4.0, and 5.0) of the second phases ($Bi_2S_3$, $Sb_2S_3$, SrS, and CaS) were synthesized by melting reaction method through mixing appropriate ratios of starting materials (CaS containing sample starts from Ca and S) in carbon-coated silica tubes (Ø ≈ 8 mm) under an Ar-filled glovebox. The tubes were sealed under high vacuum ($\sim 10^{-4}$ Torr) and slowly heated to 723 K in 12 h, then heated to 1423 K in 7 h, and soaked at this temperature for 6 h. The furnace was rocked for good mixing of the molten sample, which tends to reduce ingot bubbles and ensures homogeneous composition. The tubes were subsequently air quenched to room temperature.

PbS samples were prepared by a Bridgman crystal grown method using a single-zone furnace and synthesized by the above-mentioned sealed tubes reaction with the same heating profile, cooling from 1423 K to room temperature at a rate of 2 mm $h^{-1}$.

The spark plasma sintering (SPS) method for the preparation of samples involved the hand grinding of the melt grown ingots, to power down by mortar and pestle by hand to reduce size to smaller than 5 $mm^3$, and then mechanical mortar and pestle to reduce to smaller than 53 $\mu m^3$. The grinding was carried out inside an argon-filled glovebox. The powders subsequently were densified using a SPS system (SPS-DR 2050, Thermal Technology) at 823 K with holding time of 10 min in a Φ 20 mm graphite die under an axial compressive stress of 60 MPa in an argon atmosphere.

The obtained samples were sealed inside an evacuated silica tube with a base pressure of $\sim 10^{-4}$ Torr, and then annealed at 723 K for 15 days to evaluate thermal stability. Typical sample photographs prepared by different synthesized methods and annealing treatment are given in the Supporting Information (Figure S1).

**Physical Characterization.** *Electrical Properties.* The obtained ingots were cut into bars with the dimension of 10 mm × 3 mm × 2 mm that were used for simultaneous measurements of the Seebeck coefficient and the electrical conductivity using an Ulvac Riko ZEM-3 instrument under a helium atmosphere from room temperature to 923 K. The samples, which were measured to 923 K, were coated with a thin boron nitride layer to protect instruments from evaporated materials (see the Supporting Information for a sample photograph, Figure S1c). The longer direction coincides with the direction along which the thermal conductivity measurements were made. Heating and cooling cycles give repeatable electrical properties for a given sample. Electrical properties obtained from different slices cut from the same ingot were similar, attesting to the good homogeneity of the samples. The uncertainty of Seebeck coefficient and electrical conductivity is within 5%.

Hall coefficients were measured on a home-built system in magnetic fields ranging from 0 to 1.25 T, utilizing simple four-contact Hall-bar geometry, in both negative and positive polarity to eliminate Joule resistive errors.

*Thermal Conductivity.* The ingots obtained were cut into coins of Ø ≈ 8 mm and 1−2 mm thickness for thermal diffusivity measurements. The samples were coated with a thin layer of graphite to minimize errors on the emissivity of the material. The thermal conductivity was calculated from $k = DC_p\rho$, where thermal diffusivity coefficient $D$ was measured using the laser flash diffusivity method in a Netzsch LFA457, the data were analyzed using a Cowan model with pulse correction,[16] and heating and cooling cycles give a repeatable diffusivity for a given sample. Thermal diffusivities obtained for different slices from the same ingot are similar, where $C_p$ is the specific heat capacity, and was indirectly derived using standard sample (Pyroceram 9606) in the range 300−923 K; the $C_p$ results show good agreement with the reported values,[31] where the density $\rho$ of the sample was determined by using sample dimension and mass, and the sample density was also reconfirmed by gas pycnometer (Micromeritics AccuPyc1340) measurements. The errors in the thermal conductivity are estimated to be within 8% considering the uncertainties for $D$, $C_p$, and $\rho$. The thermal diffusion and the heat capacity data for all samples can be found as Supporting Information (Figure S5). The combined uncertainty for all measurements involved in $ZT$ determination is within 15%.

*Electron Microscopy and X-ray Diffraction.* Scanning electron microscopy (SEM) studies were performed using a Hitachi S-3400N VP-SEM equipped with an Oxford detector for energy dispersive X-ray spectroscopy (EDS). The samples used for SEM and EDS were the coins used for thermal diffusivity, and they were polished using a suspension of 50 nm $Al_2O_3$ particles. Scanning/transmission electron microscopy (S/TEM) investigations were carried out in a JEOL 2100F microscope operated at 200 kV. The thin TEM specimens were prepared by conventional standard methods. The procedures include cutting, grinding, dimpling, polishing, and Ar-ion milling on a liquid nitrogen cooling state subsequently. Samples pulverized in an agate mortar were used for powder X-ray diffraction; the powder diffraction patterns were obtained via Cu $K_\alpha$ ($\lambda$ = 1.5418 Å) radiation in a reflection geometry on an Inel diffractometer equipped with a position-sensitive detector and operating at 40 kV and 20 mA.

## RESULTS AND DISCUSSION

The designing strategy for improving the thermoelectric performance of PbS via doping and nanostructuring is described below as several rational successive steps. First, the electrical transport properties (power factor) of pure PbS prepared by a melting reaction are optimized through $PbCl_2$ doping. Second, selected metal sulfides would be used as the second phases for dispersion in the PbS matrix to lower the thermal conductivity; these are $Bi_2S_3$, $Sb_2S_3$, SrS, and CaS. Third, by choosing the proper second phase candidates, we show that a high $ZT$ is obtained through the combination of high power factor at optimized $PbCl_2$ doping level and low thermal conductivity. Fourth, the samples with optimized chemical compositions synthesized by the Bridgman crystal growth method and powder processed using SPS are shown to demonstrate the repeatability of the thermoelectric properties regardless of the preparation method. Finally, a high temperature annealing treatment of optimized samples is presented for 15 days, which showed improvement rather than deterioration of the thermoelectric properties, suggesting good thermal stability.

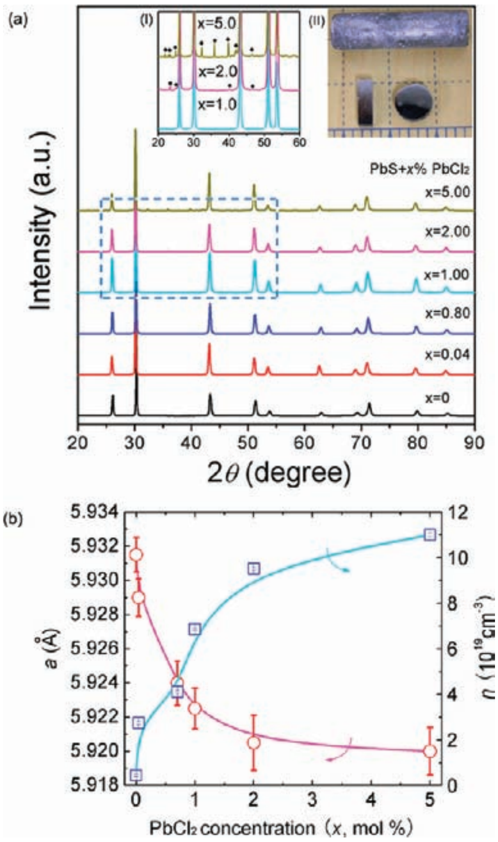

**Figure 2.** (a) Powder XRD patterns for PbS with $x$ mol % $PbCl_2$ doping, and (b) the lattice parameters and carrier density as a function of $PbCl_2$ concentration. Inset of (a): (I) enlarged PXRD pattern ranges from 20° to 60° (2$\theta$ deg), and (II) typical melting reaction ingot and samples used in this study.

**1. Pristine PbS Doped with *x* mol %$PbCl_2$.** As indicated in previous work,[16] the solid state solution limit of the electron donor dopant $PbCl_2$ in PbS is not reached even as the doping content climbs to 0.1 mol %. Therefore, to determine the solubility limit of $PbCl_2$ in PbS, we increased the $PbCl_2$ doping content up to 5.0 mol %. As shown in Figure 2a, all of the PXRD patterns can be indexed in the NaCl structure as a nearly single PbS phase. However, a small impurity phase of $PbCl_2$ can be indexed as the doping content exceeds 1.0 mol %, as shown in the expanded PXRD pattern range from 20° to 60° (2$\theta$) in the inset of Figure 2a(I), suggesting that somewhere between 1.0 and 2.0 mol % doping reaches the solubility limit. This conclusion is supported by the variation of the lattice parameters and carrier concentration as a function of $PbCl_2$, as shown in Figure 2b. The lattice parameter decreases significantly up to 1.0 mol % $PbCl_2$ doping content and beyond that decreases slowly, stabilizing as the content reaches 5.0 mol %. The lattice contraction is consistent with the radius of $Cl^-$ ions (~1.81 Å) being smaller than that of $S^{2-}$ ions (~1.84 Å) and suggests that $Cl^-$ was successfully incorporated into the PbS lattice. Also, the carrier concentrations ($n_H$) at room temperature increase rapidly from 0.44 × $10^{19}$ for pristine PbS to 6.85 × $10^{19}$ $cm^{-3}$ for the sample with 1.0 mol % $PbCl_2$ doping, and then increase more slowly with increasing doping content, reaching a maximum value of 11.6 × $10^{19}$ $cm^{-3}$ for the sample with 5.0 mol % $PbCl_2$; see Figure 2b. Collectively, the lattice parameter variation and carrier concentration indicate that the solubility limit of $PbCl_2$ in PbS ranges between 1.0 and 2.0 mol %.

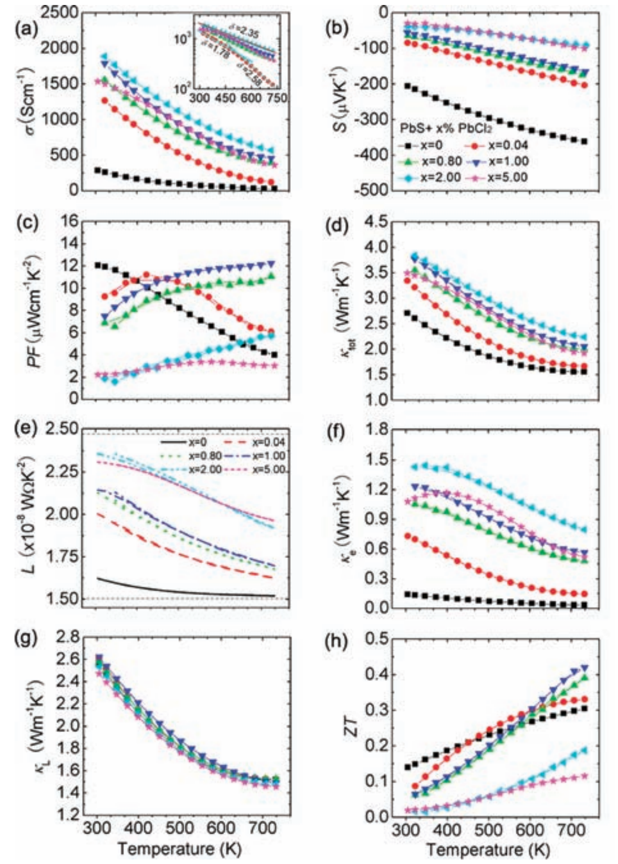

**Figure 3.** Thermoelectric properties as a function of temperature for PbS with *x* mol % $PbCl_2$ doping: (a) electrical conductivity. Inset shows conductivity data for the doped samples on logarithmic scales: (b) Seebeck coefficient; (c) power factor; (d) total thermal conductivity; (e) Lorenz number; (f) electronic thermal conductivity; (g) lattice thermal conductivity; and (h) *ZT*.

As shown in Figure 3a, the electrical conductivity of the PbS samples doped with *x* mol % $PbCl_2$ decreases with rising temperature. As the content of $PbCl_2$ rises, the room temperature electrical conductivity significantly increases from ~250 S $cm^{-1}$ for the pristine (undoped) PbS to ~1900 S $cm^{-1}$ for the sample with 2.0 mol % $PbCl_2$ doping. However, at 5.0 mol % the trends break as the electrical conductivity decreases to ~1550 S $cm^{-1}$, and this anomaly may arise from excessive impurity phase that reduces carrier mobility by increasing scattering related to $PbCl_2$ as observed in the PXRD shown in Figure 2a. There is good agreement between the measured Hall charge carrier concentrations listed in Table 1 and the room temperature electrical conductivity.

While the electrical conductivity can be effectively described by a power law of $\sigma \approx T^{-\delta}$ with $\delta$ = 2.00−2.50 for the reported doped PbTe,[25] this is not the case for the PbS samples with low doping content. This is evident in the inset in Figure 2a where the electrical conductivities of the doped samples are plotted as a function of temperature on a logarithmic scale. For the sample with lower doping content, for example, 0.04 mol % $PbCl_2$, no single power law can describe the data over the whole temperature range, and $\delta$ ranges from 1.78 at low temperature and 2.58 at high temperature. However, for the samples with higher doping, for example, 2.0 mol % $PbCl_2$, the power exponent $\delta$ becomes constant at 2.35 in the entire temperature range. This reflects the shift from nondegenerate behavior at lower doping content to a degenerate behavior at higher doping.[16]

As shown in Figure 3b, the Seebeck coefficients are negative, indicating all samples are n-type conductors. At room temperature, the Seebeck coefficient decreases with the amount of added $PbCl_2$. It varies from about −200 $\mu$V/K for the pristine PbS to −45 $\mu$V/K for the sample after 5.0 mol % $PbCl_2$ doping,

**Table 1. Transport Properties of PbS-Based Samples Prepared by the Melting Reaction with Selected Second Phases and $PbCl_2$ Doping[a]**

| samples | $n_H$ ($10^{19}$ $cm^{-3}$) | $r_H$ | $\mu_H$ ($cm^2$ $V^{-1}$ $s^{-1}$) | $S$ ($\mu$V $K^{-1}$) | $\sigma$ (S $cm^{-1}$) | $m^*(m_e)$ | $\kappa_L$ (room temp) (W $m^{-1}$ $K^{-1}$) | $\kappa_L$ (723 K) (W $m^{-1}$ $K^{-1}$) | $ZT_{max}$ |
|---|---|---|---|---|---|---|---|---|---|
| PbS | 0.44 | 1.15 | 405 | −206 | 285 | 0.45 | 2.56 | 1.52 | 0.30 |
| PbS + 0.04%$PbCl_2$ | 2.75 | 1.06 | 288 | −85 | 1265 | 0.40 | 2.61 | 1.52 | 0.33 |
| PbS + 0.80%$PbCl_2$ | 4.12 | 1.04 | 236 | −64 | 1553 | 0.39 | 2.58 | 1.53 | 0.39 |
| PbS + 1.00%$PbCl_2$ | 6.85 | 1.03 | 169 | −55 | 1856 | 0.45 | 2.62 | 1.49 | 0.42 |
| PbS + 2.00%$PbCl_2$ | 9.52 | 1.02 | 124 | −38 | 1888 | 0.37 | 2.53 | 1.48 | 0.19 |
| PbS + 5.00%$PbCl_2$ | 11.6 | 1.01 | 83 | −30 | 1533 | 0.36 | 2.47 | 1.46 | 0.12 |
| PbS + 1.0%$Bi_2S_3$ + 1.0%$PbCl_2$ | 6.56 | 1.03 | 176 | −49 | 1850 | 0.39 | 1.37 | 0.70 | 0.80 |
| PbS + 3.0%$Bi_2S_3$ + 1.0%$PbCl_2$ | 6.61 | 1.03 | 98 | −44 | 1035 | 0.36 | 1.14 | 0.60 | 0.48 |
| PbS + 5.0%$Bi_2S_3$ + 1.0%$PbCl_2$ | 6.72 | 1.04 | 55 | −61 | 587 | 0.46 | 0.76 | 0.54 | 0.47 |
| PbS + 1.0%$Sb_2S_3$ + 1.0%$PbCl_2$ | 6.55 | 1.04 | 121 | −68 | 1269 | 0.54 | 1.58 | 0.74 | 0.78 |
| PbS + 3.0%$Sb_2S_3$ + 1.0%$PbCl_2$ | 5.89 | 1.04 | 70 | −73 | 662 | 0.53 | 1.26 | 0.69 | 0.39 |
| PbS + 5.0%$Sb_2S_3$ + 1.0%$PbCl_2$ | 6.70 | 1.05 | 19 | −66 | 200 | 0.54 | 1.00 | 0.53 | 0.53 |
| PbS + 1.0%SrS + 1.0%$PbCl_2$[b] | 6.95 | 1.02 | 402 | −36 | 4731 | 0.28 | 1.92 | 1.00 | 0.58 |
| PbS + 1.0%CaS + 1.0%$PbCl_2$[b] | 6.90 | 1.03 | 254 | −56 | 2801 | 0.45 | 2.22 | 1.03 | 0.63 |
| sample[b] after annealing | 7.01 | 1.02 | 299 | −44 | 3355 | 0.37 | 2.10 | 0.94 | 0.63 |

[a] $n_H$, carrier concentration; $r_H$, Hall factor; $\mu_H$, mobility; $m^*(m_e)$, effective mass. [b] Samples prepared by the Bridgman crystal growth method.

which is consistent with an increase of the carrier concentrations induced by the substitution of $S^{2-}$ by $Cl^{-}$.

The power factor of pristine PbS shows a maximum of $\sim 12\ \mu W\ cm^{-1}\ K^{-2}$ around room temperature, which falls to $\sim 4\ \mu W\ cm^{-1}\ K^{-2}$ at 723 K, Figure 3c. The maximum of the power factor is pushed to higher temperature as the amount of n-type dopant is increased. The power factor maximum peaks at $\sim 11\ \mu W\ cm^{-1}\ K^{-2}$ at 723 K for the 0.8 mol % $PbCl_2$ doped sample. The maximum for the 1.0 mol % $PbCl_2$ doped sample peaks at $\sim 12\ \mu W\ cm^{-1}\ K^{-2}$ at 723 K.

The total thermal conductivity in the entire temperature range of measurements increases with $PbCl_2$ doping, Figure 3d. The total thermal conductivity ($\kappa_{tot}$) includes a sum of the electronic ($\kappa_e$) and lattice thermal conductivity ($\kappa_L$). The increase of the total thermal conductivity is the result of the increasing fraction of the electronic thermal conductivity ($\kappa_e$), as shown in Figure 3f. The electronic part $\kappa_e$ is directly proportional to the electrical conductivity $\sigma$ through the Wiedemann–Franz relation, $\kappa_e = L\sigma T$, where $L$ is the Lorenz number.[32] Here, it would be worth discussing in detail the two contributing parts of the total thermal conductivity. Because nanostructuring has proved to be an effective method of reducing the lattice thermal conductivity $\kappa_L$,[1] separating the electronic and lattice parts is important in studying the effect of embedded nanostructures in a host thermoelectric matrix. Generally, the lattice thermal conductivity $\kappa_L$ can be estimated by directly subtracting $\kappa_e$ from $\kappa_{tot}$ by using:

$$L_0 = \frac{\pi^2}{3}\left(\frac{k_B}{e}\right)^2 \simeq 2.45 \times 10^{-8}\ W\ \Omega\ K^{-2} \tag{1}$$

Although this may be a good estimation for the lattice thermal conductivity $\kappa_L$ at room temperature, it does not hold true for metallic materials or for heavily doped semiconductors where a strong change with temperature is observed in the chemical potential.[33] For most thermoelectric materials, the true Lorenz number is in fact lower than $L_0$ ($2.45 \times 10^{-8}\ W\ \Omega\ K^{-2}$) especially at high temperature. The Lorenz number depends on the scattering parameter $r$ and will decrease as the reduced Fermi energy $\eta$ decreases with increasing temperature. The Lorenz number can be given as:[34]

$$L = \left(\frac{k_B}{e}\right)^2 \left(\frac{(r + 7/2)F_{r+5/2}(\eta)}{(r + 3/2)F_{r+1/2}(\eta)} - \left[\frac{(r + 5/2)F_{r+3/2}(\eta)}{(r + 3/2)F_{r+1/2}(\eta)}\right]^2\right) \tag{2}$$

For the Lorenz number calculation, we should get reduced Fermi energy $\eta$ first; the calculation of $\eta$ can be derived from the measured Seebeck coefficients by using the following relationship:

$$S = \pm \frac{k_B}{e}\left(\frac{(r + 5/2)F_{r+3/2}(\eta)}{(r + 3/2)F_{r+1/2}(\eta)} - \eta\right) \tag{3}$$

where $F_n(\eta)$ is the $n$th order Fermi integral:

$$F_n(\eta) = \int_0^{\infty} \frac{\chi^n}{1 + e^{\chi - \eta}}\, d\chi \tag{4}$$

$$\eta = \frac{E_f}{k_B T} \tag{5}$$

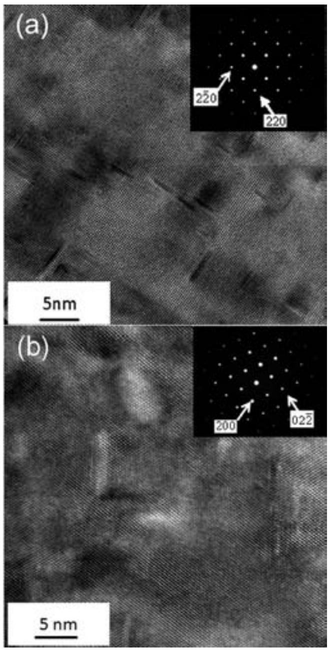

**Figure 4.** High-resolution TEM image of PbS doped with (a) 0.04 mol % and (b) 1.0 mol % $PbCl_2$. Insets show the corresponding diffraction patterns along (a) [001] and (b) [011] zone axis.

In the above equations, $k_B$ is the Boltzmann constant, $e$ is the electron charge, and $E_f$ is the Fermi energy. Meanwhile, acoustic phonon scattering has been assumed as the main carrier scattering mechanism,[16] so, $r = -1/2$.[35] The Lorenz number can be obtained by applying the calculated reduced Fermi energy $\eta$ and scattering parameter $r$ into eq 2. As shown in Figure 3e, all of the Lorenz numbers range from nondegenerate limit ($1.5 \times 10^{-8}\ W\ \Omega\ K^{-2}$) to the degenerate limit ($2.45 \times 10^{-8}\ W\ \Omega\ K^{-2}$) and show an increasing trend with doping level.[32] On the basis of the above calculation for Lorenz number, the $\kappa_L$ can be estimated by subtracting $\kappa_e$ from $\kappa_{tot}$ if no bipolar diffusion exists. If bipolar diffusion takes place, the electronic thermal conductivity $\kappa_e$ will be overestimated when both holes and electrons are present at high temperature, and an extra term (bipolar thermal conductivity, $k_{bipolar}$) then needs to be added to the total thermal conductivity. However, no upturn at high temperature was observed for any of the doped PbS samples, indicating that bipolar diffusion is negligible at these doping levels and temperatures.

After proper calculation of $\kappa_e$, we observe that the lattice thermal conductivity is nearly independent of doping; see Figure 3g. A slightly lower lattice thermal conductivity was found at 5.0 mol % $PbCl_2$ doping, which may be caused by phonon scattering associated with the impurity phases related to the excess $PbCl_2$. Combining the results of the electrical and thermal transport properties, a maximum $ZT$ value of 0.42 was obtained for the 1.0 mol % $PbCl_2$ doped sample, Figure 3h; this value is 40% higher than the high $ZT$ value of 0.30 for the pristine PbS sample. Therefore, the optimum doping level is achieved at ~1.0 mol % $PbCl_2$ content.

The TEM images of the 0.04 and 1.0 mol % $PbCl_2$ doped samples are shown in Figure 4a and b, respectively. The inset electron diffraction patterns were collected by an aperture including several precipitates and part of matrix and clearly show that the PbS structure (i.e., crystal symmetry) is not changed by doping of $PbCl_2$. The precipitates are plate-like as confirmed by

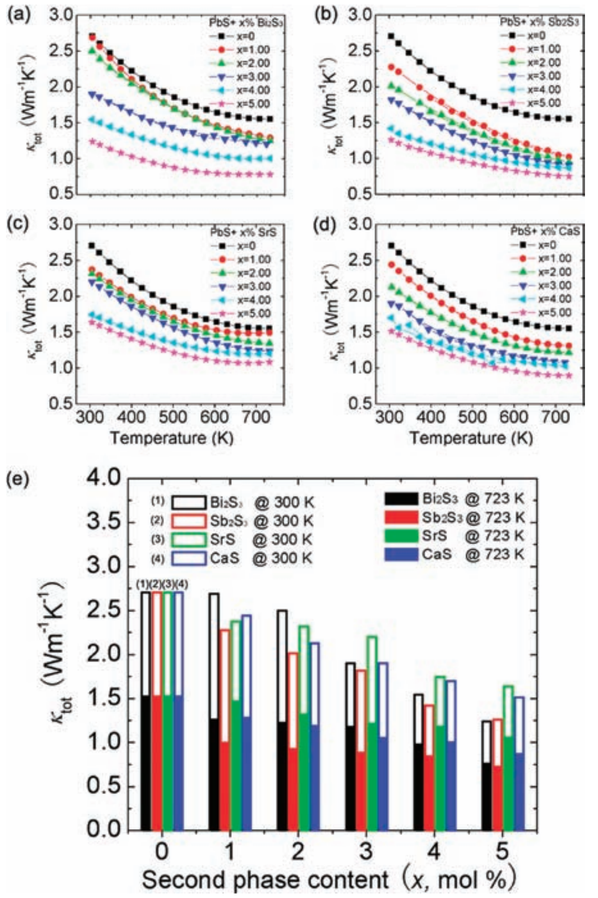

**Figure 5.** Total thermal conductivities as a function of temperature for PbS with different contents of second phase candidates: (a) PbS with $x$ mol % $Bi_2S_3$; (b) PbS with $x$ mol % $Sb_2S_3$; (c) PbS with $x$ mol % SrS; and (d) PbS with $x$ mol % CaS. (e) The comparisons of thermal conductivity at 300 and 723 K.

high-resolution images along [001], [011] (Figure 4), and [11$\bar{2}$] (see Supporting Information Figure S2) zone axes. Along the [011] zone axis, the strips appear to have a common shape; on the other hand, these precipitates project oval/spherical shapes along the [011] and [11$\bar{2}$] directions. The typical size for these precipitates is in the range of 2−20 nm. According to observations along different zone axes, there is a preferred growth orientation along [001] of these plate-like precipitates. As indicated above by the negligible reduction of the lattice thermal conductivity (Figure 3g), the plate-like precipitates observed here for the $PbCl_2$ doped samples do not seem effective in enhancing phonon scattering. The main reason is that the plate-like precipitates are probably $PbS_{1-x}Cl_x$ with a small $x$ value that cannot strongly scatter phonons.[29] However, as we will demonstrate below, highly effective phonon scattering is achieved with the binary sulfide phases of $Bi_2S_3$, $Sb_2S_3$, SrS, and CaS.

**2. Nanostructuring PbS with *x* mol %$Bi_2S_3$ ($Sb_2S_3$, SrS, and CaS).** After having characterized the full thermoelectric properties of the pristine PbS system and its n- doped samples using $PbCl_2$ as the dopant, we explored the introduction of selected second phases as potential nanostructures in the undoped PbS matrix. First, we studied the undoped samples of PbS with $x$ mol % $Bi_2S_3$ ($Sb_2S_3$, SrS, and CaS). Our goal was to investigate how small additions of $Bi_2S_3$, $Sb_2S_3$, SrS, and CaS nanostructures impacted the lattice thermal conductivity. This was followed with $PbCl_2$ doping of selected systems for $ZT$ optimization. We studied samples with $x$ = 0, 1.0, 2.0, 3.0, 4.0, and 5.0.

The PXRD patterns of the PbS with $x$ mol % $Bi_2S_3$ ($Sb_2S_3$, SrS, and CaS) systems show no impurity phases even though the contents of the second phases increase up to 5.0 mol % (see Supporting Information Figure S3). As shown in Figure 5a−d, the thermal conductivity is significantly reduced by introducing the second phases, and this occurs over the entire temperature range. The thermal conductivity at 300 K is reduced by about 4%, 16%, 12%, and 9% through introducing 1.0 mol % $Bi_2S_3$, $Sb_2S_3$, SrS, and CaS, respectively. The thermal conductivity at 723 K, however, is spectacularly reduced by ∼50%, 52%, 30%, and 42% by introducing 5.0 mol % $Bi_2S_3$, $Sb_2S_3$, SrS, and CaS, respectively; see Figure 5e.

For the undoped PbS pristine crystals as indicated in Figure 3d and g and discussed above, we can estimate that at 300 K the thermal conductivity originating from the phonon contribution ($\kappa_L/\kappa_{tot}$) exceeds 95% of the total thermal conductivity. Similarly, at 723 K, the ratio of $\kappa_L/\kappa_{tot}$ for the undoped high-resistivity PbS is about 98%, indicating that the thermal transport is dominated by the phonons. Correspondingly, the total thermal conductivity for the undoped samples with second phases of $Bi_2S_3$, $Sb_2S_3$, SrS, and CaS essentially represents the lattice thermal conductivity. Thus, the above results demonstrate that lattice thermal conductivity can be reduced effectively by the selected aforementioned second phases, especially at high temperature.

**3. Samples of PbS with *x* mol % $Bi_2S_3$ ($Sb_2S_3$, SrS, and CaS) Doped with 1.0 mol % $PbCl_2$.** The thermoelectric properties of PbS samples with varying content of $Bi_2S_3$, $Sb_2S_3$, SrS, and CaS were evaluated at fixed 1.0 mol % $PbCl_2$ doping concentration, which was shown above to maximize the power factor. Starting with the $Bi_2S_3$ containing system, the PXRD patterns show a single phase that can be indexed in the NaCl structure type regardless of $Bi_2S_3$ fraction up to 5 mol %, Figure 6a. With increasing $Bi_2S_3$ fraction, the electrical conductivities in the entire temperature range of measurements show a decreasing trend (Figure 6b); however, the Seebeck coefficients show negligible changes (Figure 6c). This suggests the carrier concentration is similar for all samples (as controlled by the $PbCl_2$ concentration) and the rising fraction of $Bi_2S_3$ as a second phase degrades the electron mobility, Table 1. As compared to similarly doped PbS samples, those containing 1.0 mol % $Bi_2S_3$ and doped with 1.0 mol % $PbCl_2$ show only a small reduction in electrical conductivity and nearly no change of Seebeck coefficient, resulting in a similar power factor of ∼12 $\mu$W cm$^{-1}$ K$^{-2}$.

The total thermal conductivity of this sample series shows a significant decrease with increasing $Bi_2S_3$ fraction (Figure 6e). This falling trend is also reflected in the lattice thermal conductivity (Figure 6g), indicating that the dispersed $Bi_2S_3$ phase is highly effective in reducing the lattice thermal conductivity. At room temperature, the lattice thermal conductivity significantly decreases from ∼2.55 W m$^{-1}$ K$^{-1}$ for the pristine PbS to ∼1.75 W m$^{-1}$ K$^{-1}$ for the sample with 1.0 mol % $Bi_2S_3$, and further decreases to ∼0.76 W m$^{-1}$ K$^{-1}$ as the $Bi_2S_3$ contents climb to 5.0 mol %. Correspondingly, the lattice thermal conductivity at 723 K decreases from ∼1.50 W m$^{-1}$ K$^{-1}$ for the pristine PbS to ∼0.82 and ∼0.54 W m$^{-1}$ K$^{-1}$ as the $Bi_2S_3$ content rises from 1.0 to 5.0 mol %, respectively. These values are lower than that of PbS with 16.0 mol % PbTe.[16]

As shown in Figure 6h, the maximum of $ZT$ value is observed for the PbS sample with 1.0 mol % $Bi_2S_3$ and 1.0 mol % $PbCl_2$

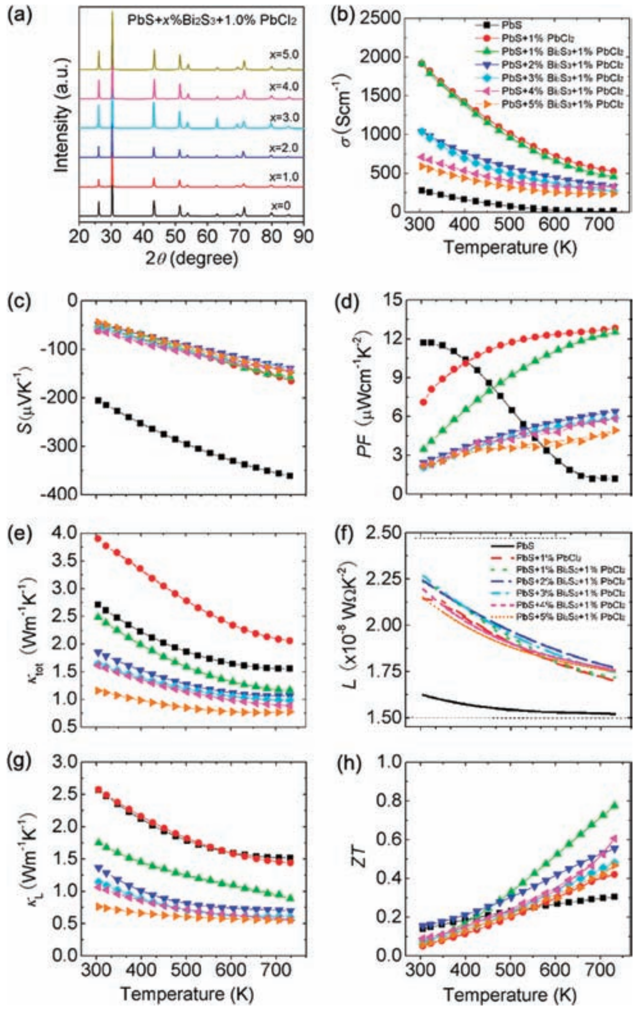

**Figure 6.** (a) Powder XRD and thermoelectric properties as a function of temperature for PbS with *x* mol % $Bi_2S_3$ and 1.0 mol % $PbCl_2$ doping: (b) electrical conductivity; (c) Seebeck coefficient; (d) power factor; (e) total thermal conductivity; (f) Lorenz number; (g) lattice thermal conductivity; and (h) *ZT* values. The highest value is exhibited by the PbS with 1.0 mol % $Bi_2S_3$ doped with 1.0 mol % $PbCl_2$ sample.

doping reaching ~0.80 at 723 K with no signs of saturation. This value exceeds the previously reported value of ~0.72 at 710 K for PbS with 8.0 mol % PbTe and 0.067 mol % $PbCl_2$ doping.[16] The experimental results indicate that the introduction of only 1.0 mol % $Bi_2S_3$ inclusion phase combined with n-type $PbCl_2$ doping significantly boosts the thermoelectric properties of PbS.

$Sb_2S_3$ was selected as another inclusion phase candidate related to $Bi_2S_3$ to investigate whether the size of the metal (e.g., Bi vs Sb) as compared to that of Pb had a marked effect on the thermoelectric properties of PbS and particularly on the lattice thermal conductivity. The results show that all electrical and thermal transport behavior (see Supporting Information Figure S4) for the PbS samples, with $Sb_2S_3$ as dispersion phase and 1.0 mol % $PbCl_2$ doping, is very similar to that of $Bi_2S_3$. For this batch of $Sb_2S_3$-containing samples, a maximum *ZT* value of 0.78 was obtained for the sample 1.0 mol % $Sb_2S_3$ and 1.0 mol % $PbCl_2$ doping.

To assess the repeatability of the high performance, samples with the same composition (PbS + 1.0 mol % $Bi_2S_3$/$Sb_2S_3$ + 1.0 mol % $PbCl_2$) were prepared by Bridgman crystal growth as an alternative preparation method. As shown in Figure 7, all electrical and thermal transport properties for the samples prepared by the Bridgman crystal growth method are very similar to those prepared by the so-called melting reaction method. As shown in Figure 7f, the maximum *ZT* values at 723 K for the samples with 1.0 mol % $Bi_2S_3$ and $Sb_2S_3$ and with 1.0 mol % $PbCl_2$ doping reach 0.79 and 0.76, respectively. The results demonstrate that the samples prepared by the Bridgman crystal growth method can reach the same figures of merit as that of the samples prepared by the melting reaction, indicating that the high performance in this study is robust and not overly sensitive to the synthesis method used.

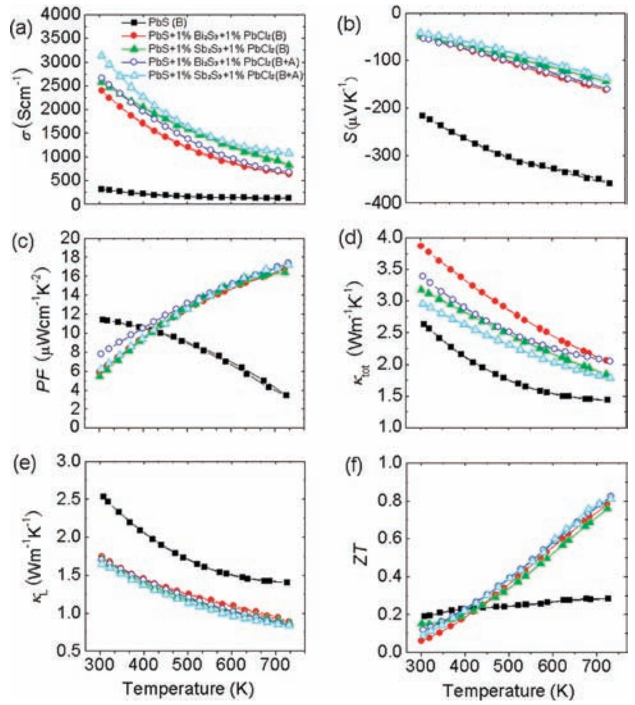

**Figure 7.** Thermoelectric properties as a function of temperature for PbS with 1.0 mol % $Bi_2S_3$($Sb_2S_3$) and doped with 1.0 mol % $PbCl_2$ doping: (a) electrical conductivity; (b) Seebeck coefficient; (c) power factor; (d) total thermal conductivity; (e) lattice thermal conductivity; and (f) *ZT*. "B" presents the samples prepared by the Bridgman method; "B + A" presents the samples prepared by the Bridgman method followed by annealing treatment at 723 K for 15 days.

To check whether the high performance was stable at an elevated temperature applied for a given duration of time, we subjected all of the high performance samples prepared by the Bridgman crystal growth method to a 15 days annealing treatment at 723 K. As shown in Figure 7f, the *ZT* values for the annealed samples (marked by open symbols) not only did not deteriorate but improved. The improvement of *ZT* values after annealing treatment is caused by the further reduction in thermal conductivity (Figure 7d) and the nearly unchanged power factor (Figure 7c). The good stability of the power factor after the annealing treatment derives from a small increase in electrical conductivity (Figure 7a) and a corresponding small decrease in the Seebeck coefficient (Figure 7b), which indicate a small increase in carrier concentration (Table 1). This may be due to slight loss of sulfur from the PbS samples during annealing. Nevertheless, the annealed samples showed no visible changes such as bubbles, cracks, or color changes on the surface, and appeared to be of the same quality as before annealing (see the Supporting Information

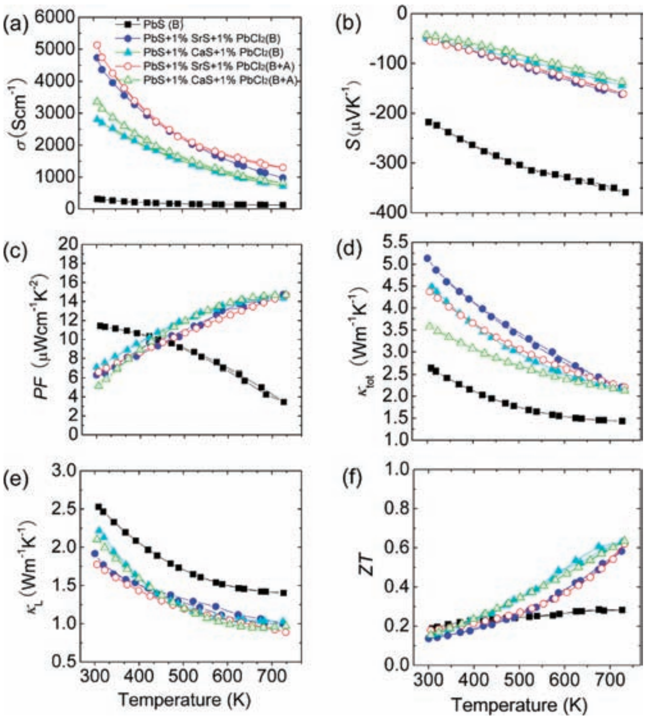

**Figure 8.** Thermoelectric properties as a function of measurement temperature for PbS with 1.0 mol % SrS(CaS) and doped with 1.0 mol % $PbCl_2$ doping: (a) electrical conductivity; (b) Seebeck coefficient; (c) power factor; (d) total thermal conductivity; (e) lattice thermal conductivity; and (f) *ZT*. "B" presents the samples prepared by Bridgman method; "B + A" presents the samples prepared by the Bridgman method followed by annealing treatment at 723 K for 15 days.

for photographs of annealed samples, Figure S1d). This behavior is similar to the enhanced properties observed for annealed $Ag_{0.8}Pb_{22.5}SbTe_{20}$,[36] in which the inherent nanostructuring is improved by the annealing treatment, further reducing the thermal conductivity.

PbS samples with 1.0 mol % SrS and CaS content were also prepared by Bridgman crystal growth method and annealed for 15 days to evaluate the thermal stability. The SrS/CaS-containing samples show higher electrical conductivities than the $Bi_2S_3$/$Sb_2S_3$ containing samples, Figures 7a and 8a, whereas they exhibit nearly the same lattice thermal conductivity (Figure 8e). As shown in Table 1, the SrS/CaS-containing samples show higher electron mobilities than the $Bi_2S_3$/$Sb_2S_3$-containing ones and are nearly comparable to those of a similarly doped pristine PbS sample. The high carrier mobility and low lattice thermal conductivity for SrS/CaS containing samples may be mediated by the presence of coherent or semicoherent interfaces between the PbS matrix and the isostructural rock salt SrS/CaS phases, which exhibit a small lattice mismatch, for example: $a_{PbS}$ = 5.9340 Å, $a_{SrS}$ = 6.0079 Å, $a_{CaS}$ = 5.6860 Å. As shown in Figure 8f, the maximum *ZT* values at 723 K for the samples with 1.0 mol % SrS and CaS and with 1.0 mol % $PbCl_2$ doping reach 0.58 and 0.63, respectively. The *ZT* values for SrS/CaS containing samples are lower than that of $Bi_2S_3$/$Sb_2S_3$ containing samples. As shown in Figure 8, the annealed samples (marked by open symbols) also show an excellent thermal stability.

The Seebeck coefficients of the $PbCl_2$-doped samples presented here with or without the added metal sulfide phases were checked as a function of carrier concentration at room temperature.

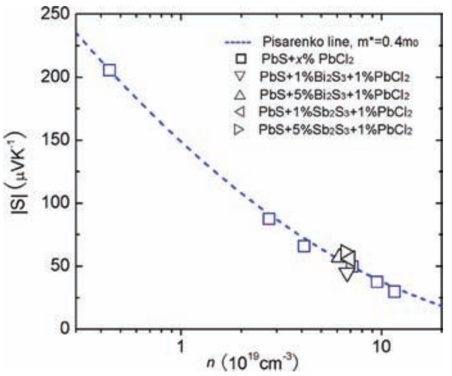

**Figure 9.** Pisarenko plot at 300 K. Seebeck coefficient as a function of carrier concentration. The line corresponds to the theoretically expected curve for the pristine PbS with $m^* \approx 0.4m_o$. The excellent agreement suggests that $PbCl_2$ doping levels and second phases have no marked effects in perturbing the electronic density of states of PbS.

The well-established Pisarenko relation of Seebeck coefficient and carrier concentration assuming a parabolic band and an acoustic phonon scattering mechanism can give a good description for the experimental data. In this approximation, the carrier concentration was approximated by the relationship:[13]

$$n = 4\pi\left(\frac{2m^*k_BT}{h^2}\right)^{3/2}\frac{F_{1/2}(\eta)}{r_H} \tag{6}$$

and the Seebeck coefficient, given by eq 3. In the above equation, $m^*$ is the effective mass, and $h$ is the Planck constant. Here, it should be noted that the Hall factor, $r_H$, which takes into account band anisotropy and relaxation time of carriers moving along and across the principal conduction axis of the Fermi surface, will be about unity for parabolic bands and a spherical Fermi surface.[37] The scattering factor, $r$, is $-1/2$ because acoustic phonon scattering has been assumed as the main carrier scattering mechanism near room temperature. Using eqs 6 and 3, we varied the values of reduced Fermi energy $\eta$ to generate carrier concentration $n$ and Seebeck coefficient $S$ pairs on the assumption of an effective mass ~0.4 $m_o$ for PbS.[16] The results are shown as the dotted line in Figure 9, and as compared to several PbS samples with $x$ mol % $PbCl_2$ doping, the carrier concentration increases from $0.44 \times 10^{19}$ cm$^{-3}$ for pristine PbS to $2.75 \times 10^{19}$, $4.12 \times 10^{19}$, $6.85 \times 10^{19}$, $9.52 \times 10^{19}$, and $11.6 \times 10^{19}$ cm$^{-3}$ as the doping contents increases to 0.04, 0.8, 1.0, 2.0, and 5.0, respectively. It is noteworthy that the Seebeck coefficients for the samples with 1.0 and 5.0 mol % $Bi_2S_3$ ($Sb_2S_3$) and 1.0 mol % $PbCl_2$ doping show an excellent agreement with those pristine PbS within the studied carrier concentration range.

The experimentally determined values and the Pisarenko line show excellent agreement, suggesting that the electron scattering mechanism is not greatly affected by $PbCl_2$ doping or the nanostructuring second phases and indicates no particular enhancement of the Seebeck coefficient by resonant scattering. Therefore, a marked effect of doping on the density of states of the PbS matrix is ruled out in this work. Therefore, it can be concluded that the present thermoelectric properties of PbS are enhanced by optimizing power factor through tuning carrier concentration across a single conduction band (occurring at the L point of the Brillouin zone)[38] and particularly by reducing the lattice thermal conductivity through nanostructuring with appropriate second phases.

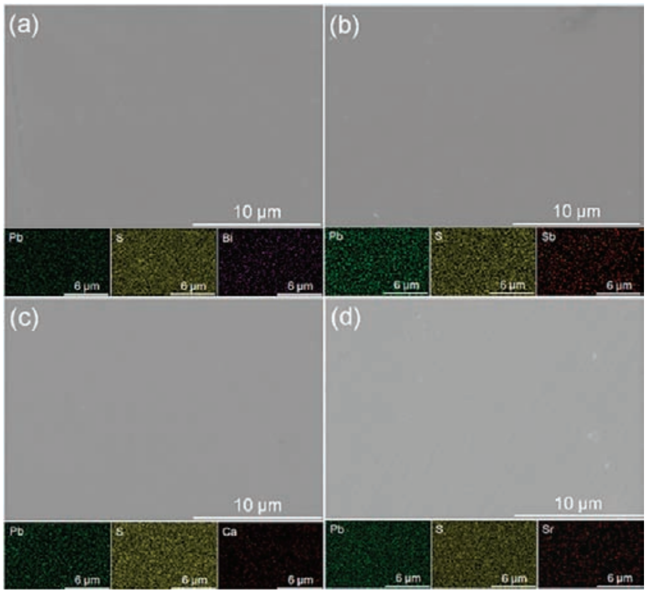

**Figure 10.** Scanning electron microscopy images for (a) PbS with 1.0 mol % $Bi_2S_3$ and doped with 1.0 mol % $PbCl_2$; (b) PbS with 1.0 mol % $Sb_2S_3$ and doped with 1.0 mol % $PbCl_2$; (c) PbS with 1.0 mol % CaS and doped with 1.0 mol % $PbCl_2$; and (d) PbS with 1.0 mol % SrS and doped with 1.0 mol % $PbCl_2$. The SEM microscale images indicate no second phase, and composition segregations can be observed. Insets show element distributions determined by energy dispersive X-ray spectroscopy (EDX) in the lower images. The elemental maps indicate a homogeneous distribution of the second phases in PbS.

The composition of the high performance samples with the optimized content of dispersed second phases (1.0 mol %) and $PbCl_2$ doping level (1.0 mol %) was examined using elemental mapping in a scanning electron microscope. The elemental distributions determined by energy dispersive X-ray spectroscopy (EDX) indicate that all of the elements are homogeneously distributed throughout the samples, Figure 10.

The nanostructures of $Bi_2S_3$ and $Sb_2S_3$ precipitates were investigated by TEM. The low magnification images along the [011] zone axis of both samples show the dark contrast of precipitates, as shown in Figure 11a and b. The shapes of these precipitates are spherical rather than the plate-like features appearing in the $PbCl_2$ doped PbS samples. Both $Bi_2S_3$- and $Sb_2S_3$-containing samples, shown in Figure 11, have similar shape and size of precipitates. The element analysis of the precipitates was carried out on the PbS with 1.0 mol % $Bi_2S_3$ and PbS with 1.0 mol % $Sb_2S_3$ sample by means of EDS. The STEM mode was utilized to achieve a probe as small as 1 nm and accommodate the size of the precipitates. The spectra were obtained by focusing the beam on the selected precipitate structures, as shown in Figure 12a and b. The signals are dominated by the contribution of the PbS matrix in which the precipitates are embedded. However, by carefully selecting thin areas to take the spectrum, the peaks of Bi/Sb can still be identified in these two samples respectively. Moreover, the high-resolution TEM images shown in Figure 13a and b further confirm the shape and size of the precipitates. In Figure 13a, the common modulation caused by the different stacking directions between the precipitates and the matrix can be seen. Therefore, the inclusion of $Bi_2S_3$ and $Sb_2S_3$ creates extensive nanoprecipitates, which are responsible for the large reductions in lattice thermal conductivity discussed above.[29]

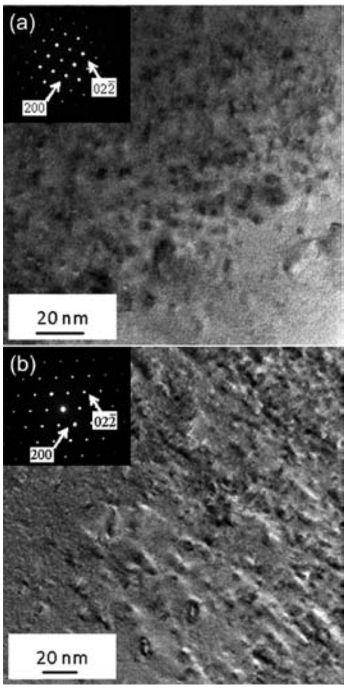

**Figure 11.** Low magnification TEM images of (a) PbS with 1.0 mol % $Bi_2S_3$ and doped with 1.0 mol % $PbCl_2$ and (b) PbS with 1.0 mol % $Sb_2S_3$ and doped with 1.0 mol % $PbCl_2$. The insets show the diffraction patterns and [011] as zone axis. The nanostructure size ranges from 3 to 15 nm on average.

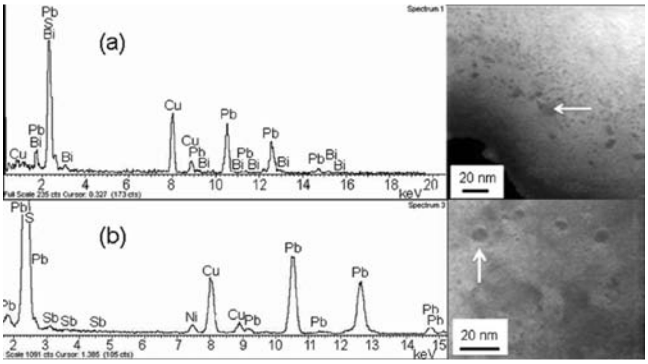

**Figure 12.** EDS spectra of typical precipitates in the samples of PbS with (a) 1.0 mol % $Bi_2S_3$ and 1.0 mol % $Sb_2S_3$. The corresponding STEM images are shown as insets.

**4. Samples of PbS with 1.0 mol % $Bi_2S_3$ ($Sb_2S_3$) Doped with 1.0 mol % $PbCl_2$ Prepared by Different Synthesis Methods.** The results presented above show that the *ZT* values for all samples have an increasing trend with temperature with no sign of saturation or topping in the Seebeck coefficient in the entire measurement range. This indicates the absence of significant bipolar diffusion up to 723 K, which is also confirmed by the temperature dependence of the thermal conductivity presented above. Because the energy band gap for lead chalcogenides shows the well-known anomalous increase with temperature,[39,40] we can expect the band gap of PbS to be larger than 0.41 eV[16] at elevated temperature. This causes the onset of intrinsic conduction to higher temperatures, thereby suppressing bipolar conduction. The reason for the band gap increase may be related to

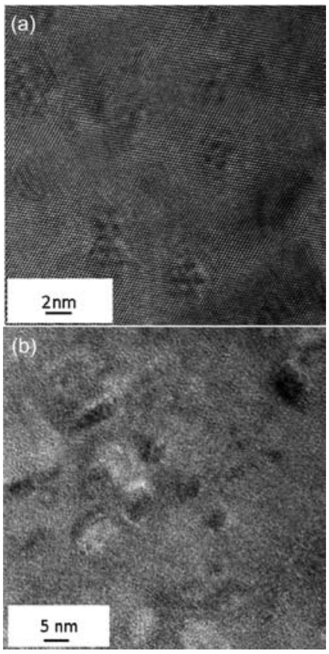

**Figure 13.** High-resolution TEM images of (a) PbS with 1.0 mol % $Bi_2S_3$ and doped with 1.0 mol % $PbCl_2$, with modulation due to different stacking directions between matrix and precipitates and (b) PbS with 1.0 mol % $Sb_2S_3$ and doped with 1.0 mol % $PbCl_2$. Both of them exhibit comparable spherical/oval-like shape and the common size range from 2 to 10 nm.

the recent discovery that the Pb atoms are in fact displaced off the octahedron center in the rock salt structure, and with the displacement increasing with rising temperature.[41] Because of the negligible bipolar diffusion, the *ZT* values may continue to rise with increasing temperature, and for this reason measurements on selected samples were extended to a temperature of 923 K. These measurements were carried out for selected high *ZT* samples after coating them with a thin boron nitride (BN) layer to protect instruments from evaporated materials.

Figure 14 shows all of the transport properties up to 923 K for the samples prepared separately by (a) melting reaction (marked by "M" in the figures), (b) Bridgman crystal growth method (B), and (c) powder processed spark plasma sintering (S). In addition, for comparison, the thermoelectric properties of a previously described sample (PbS + 3.0 mol % PbTe + 0.1 mol % $PbCl_2$)[16] prepared by the melting reaction are also plotted in Figure 14.

The electrical conductivities of all samples exhibit the same temperature-dependent trend, but the SPS processed (SPSed) samples exhibit a lower electrical conductivity. Because all samples have similar carrier concentration, the reduction in electrical conductivity is attributed to enhanced grain boundary scattering.[42,43] Remarkably, no sign of saturation or topping in the Seebeck coefficient is evident at high temperature up to 923 K; see Figure 14b. The power factors (Figure 14c) peak at high temperature except for the samples prepared by the Bridgman crystal growth method. Interestingly, the SPSed samples show a lower total thermal conductivity (Figure 14d) and lattice thermal conductivity (Figure 14g) than those of the melting reaction and the Bridgman crystal growth. The present results indicate that the lattice thermal conductivity can be greatly reduced by the second phase dispersion, and then further reduced (thought to a less degree) by grain boundary scattering. The further reduction of lattice thermal conductivity is attributed to grain boundary scattering of phonons whose wavelength is comparable to the grain size.[43]

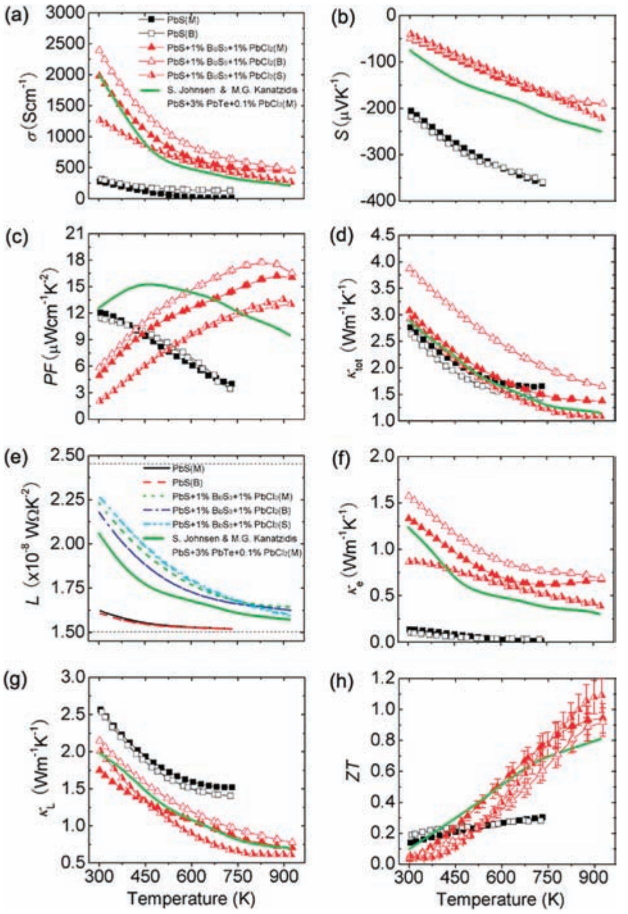

**Figure 14.** Thermoelectric properties as a function of temperature of PbS with 1.0 mol % $Bi_2S_3$ and doped 1.0 mol % $PbCl_2$: (a) electrical conductivity; (b) Seebeck coefficient; (c) power factor; (d) total thermal conductivity; (e) Lorenz number; (f) electronic thermal conductivity; (g) lattice thermal conductivity; and (h) *ZT*. "M" presents the sample prepared by the melting reaction, "B" the Bridgman method, and "S" the SPS powder processing method.

As is shown in Figure 14h, all samples exhibit high *ZT* values at 923 K, and exceed the value of 0.81 of the PbS with 3.0 mol % PbTe doped with 0.1 mol % $PbCl_2$ sample. As compared to the latter sample, the present higher *ZT* values are attributed to a high power factor achieved through optimizing the doping level and a lower thermal conductivity. The *ZT* value of 0.92 at 923 K has been obtained for melting reaction samples with the composition of 1.0 mol % $Bi_2S_3$ doped with 1.0 mol % $PbCl_2$. This high *ZT* value is matched by that of the sample with the same composition prepared by the Bridgman crystal growth method; that is, *ZT* values reach 0.95 at 923 K. Because of the further reduction of lattice thermal conductivity resulting from grain boundary scattering, the *ZT* value has been further enhanced by the SPS technique, reaching 1.1 at 923 K for the SPSed $Bi_2S_3$-containing sample.

For the $Sb_2S_3$-containing samples prepared separately by melting reaction, Bridgman crystal growth method, and spark plasma sintering, all of the electrical and thermal transport properties measured up to 923 K are very similar to those of the $Bi_2S_3$ containing ones, Figure 15. The *ZT* value of 0.91 at 923 K was

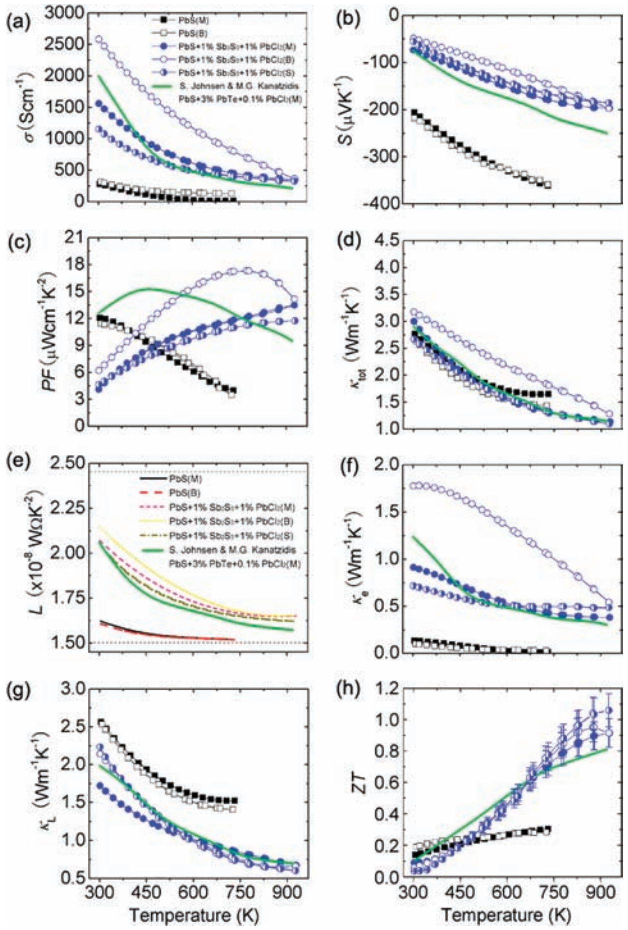

**Figure 15.** Thermoelectric properties as a function of temperature of PbS with 1.0 mol % $Sb_2S_3$ and 1.0 mol % $PbCl_2$ doping: (a) electrical conductivity; (b) Seebeck coefficient; (c) power factor; (d) total thermal conductivity; (e) Lorenz number; (f) electronic thermal conductivity; (g) lattice thermal conductivity; and (h) *ZT*. "M" presents the sample prepared by the melting reaction, "B" the Bridgman method, and "S" the SPS powder processing method.

obtained for melting reaction samples with 1.0 mol % $Sb_2S_3$ doped with 1.0 mol % $PbCl_2$. This high *ZT* value is confirmed by the sample with the same composition prepared by the Bridgman crystal growth method; that is, the *ZT* value reaches 0.94 at 875 K. The *ZT* value is further enhanced through powder processing by the SPS technique, reaching 1.06 at 923 K for the SPSed $Sb_2S_3$-containing sample, as shown in Figure 15h. Indeed, it would appear that the thermoelectric performance can be boosted by decreasing grain sizes.[3] The suppression of lattice thermal conductivity ($\kappa_L$) at high temperature due to grain boundary scattering is often negated by the deterioration of carrier mobility ($\mu$) and electrical conductivity. Because *ZT* can be enhanced by the increasing ratio of electrical conductivity and thermal conductivity, $\sigma/\kappa$, higher *ZT* values for optimized samples could be anticipated by achieving a maximum in the $\sigma/\kappa$ ratio through tuning the volume fraction of grain boundaries.

## CONCLUDING REMARKS

We demonstrated that n-type PbS, a Te-free material and inexpensive material, can achieve high *ZT* values of 1.1 at 923 K. The high performance of PbS was accomplished by shifting the power factor maximum to high temperature through tuning of the carrier concentration and reducing the lattice thermal conductivity through introduction of nanostructured second phases. We have identified a highly effective type of nanostructuring using suitably selected second phases such as $Bi_2S_3$ and $Sb_2S_3$ coupled with powder SPS processing. The high performance is characterized by a good repeatability and thermal stability and can be attained by different preparation methods and annealing treatments. The promising thermoelectric properties indicate that PbS could be a robust alternative for PbTe and PbSe thermoelectric materials.

Higher thermoelectric performance from PbS would be expected by (a) increasing the Seebeck coefficient and the power factor through the incorporation of elements forming resonance states such as electronic band structure modifications,[5] and (b) obtaining a maximum of $\sigma/\kappa$ through optimizing grain sizes with the SPS technique; and (c) with better compositions using nanodispersed phases further reducing the lattice thermal conductivity. The lowest lattice thermal conductivity for the best performing sample observed in this work is ~0.62 W m$^{-1}$ K$^{-1}$, which is the lowest value ever reported for PbS. While this is still higher than the "minimal lattice thermal conductivity" value of ~0.36 W m$^{-1}$ K$^{-1}$ for bulk PbTe as calculated by the approach of Cahill,[44] it seems to leave room for a further reduction, justifying even higher *ZT* values.

## ASSOCIATED CONTENT

**S Supporting Information.** Photos of typical high performance PbS-based samples prepared with different methods (Figure S1); the high-resolution TEM image of PbS doped with 1.0 mol % $PbCl_2$ (Figure S2); powder XRD patterns for PbS with different content of second phase candidates (Figure S3); powder XRD and thermoelectric properties as a function of measurement temperature for PbS with *x* mol % $Sb_2S_3$ and doped with 1.0 mol % $PbCl_2$ (Figure S4); and thermal diffusivity and heat capacity data for all samples in this Article (Figure S5). This material is available free of charge via the Internet at http://pubs.acs.org.

## AUTHOR INFORMATION

### Corresponding Author

m-kanatzidis@northwestern.edu

## ACKNOWLEDGMENT

This material is based upon work supported as part of the Revolutionary Materials for Solid State Energy Conversion, an Energy Frontier Research Center funded by the U.S. Department of Energy, Office of Science, Office of Basic Energy Sciences under Award Number DE-SC0001054. Part of this work was supported by grant CBET-1048728 NSF/DOE-EERE Thermoelectrics Partnership program (L.Z.). This work was also supported by the U.S. Department of Energy, Office of Science under Contract No. DE-AC02-06CH11357. Transmission electron microscopy work was performed in the (EPIC) (NIFTI) (Keck-II) facility of NUANCE Center at Northwestern University. The NUANCE Center is supported by NSF-NSEC, NSF-MRSEC, Keck Foundation, the State of Illinois, and Northwestern University.

## REFERENCES

(1) (a) Kanatzidis, M. G. *Chem. Mater.* **2010**, *22*, 648. (b) Sootsman, J. R.; Chung, D.-Y.; Kanatzidis, M. G. *Angew. Chem., Int. Ed.* **2009**, *48*, 8616. (c) Kanatzidis, M. G. *Semicond. Semimetals* **2001**, *69*, 51.

(2) (a) Li, J.-F.; Liu, W. S.; Zhao, L.-D.; Zhou, M. *NPG Asia Mater.* **2010**, *2*, 152. (b) Snyder, J. G.; Toberer, E. S. *Nat. Mater.* **2008**, *7*, 105. (c) Chen, G.; Dresselhaus, M. S.; Dresselhaus, G.; Fleurial, J.-P.; Caillat, T. *Int. Mater. Rev.* **2003**, *48*, 45. (d) Dresselhuas, M. S.; Chen, G.; Tang, M.; Yang, R.; Lee, H.; Wang, D.; Ren, Z.; Fleurial, J.; Gogna, P. *Adv. Mater.* **2007**, *19*, 1043.

(3) Poudel, B.; Hao, Q.; Ma, Y.; Lan, Y.; Minnich, A.; Yu, B.; Yan, X.; Wang, D.; Muto, A.; Vashaee, D.; Chen, X.; Liu, J.; Dresselhaus, M. S.; Chen, G.; Ren, Z. F. *Science* **2008**, *320*, 634.

(4) Hsu, K. F.; Loo, S.; Guo, F.; Chen, W.; Dyck, J. S.; Uher, C.; Hogan, T.; Polychroniadis, E. K.; Kanatzidis, M. G. *Science* **2004**, *303*, 818.

(5) Heremans, J. P.; Jovovic, V.; Toberer, E. S.; Saramat, A.; Kurosaki, K.; Charoenphakdee, A.; Yamanaka, S.; Snyder, G. J. *Science* **2008**, *321*, 554.

(6) Cook, B. A.; Kramer, M. J.; Wei, X.; Harringa, J. L.; Levin, E. M. *J. Appl. Phys.* **2007**, *101*, 053715.

(7) Pei, Y. Z.; Shi, X. Y.; LaLonde, A.; Wang, H.; Chen, L. D.; Snyder, G. J. *Nature* **2011**, *473*, 66.

(8) (a) Androulakis, J.; Hsu, K.-F.; Pcionek, R.; Kong, H.; Uher, C.; D'Angelo, J. J.; Downey, A.; Hogan, T.; Kanatzidis, M. G. *Adv. Mater.* **2006**, *18*, 1170. (b) Ahn, K.; Han, M. K.; He, J. Q.; Androulakis, J.; Ballikaya, S.; Uher, C.; Dravid, V. P.; Kanatzidis, M. G. *J. Am. Chem. Soc.* **2010**, *132*, 5227. (c) Gueguen, A.; Poudeu, P. F. P.; Li, C. P.; Moses, S.; Uher, C.; He, J. Q.; Dravid, V.; Paraskevopoulos, K. A.; Kanatzidis, M. G. *Chem. Mater.* **2009**, *21*, 1683. (d) Han, M. K.; Hoang, K.; Kong, H. J.; Pcionek, R.; Uher, C.; Paraskevopoulos, K. M.; Mahanti, S. D.; Kanatzidis, M. G. *Chem. Mater.* **2008**, *20*, 3512.

(9) Poudeu, P. F. P.; D'Angelo, J. J.; Downey, A. D.; Short, J. L.; Hogan, T. P.; Kanatzidis, M. G. *Angew. Chem., Int. Ed.* **2006**, *45*, 3835.

(10) (a) Androulakis, J.; Lin, C.-H.; Kong, H.-J.; Uher, C.; Wu, C.-I.; Hogan, T.; Cook, B. A.; Caillat, T.; Paraskevopoulos, K. M.; Kanatzidis, M. G. *J. Am. Chem. Soc.* **2007**, *129*, 9780. (b) Ahn, K.; Li, C. P.; Uher, C.; Kanatzidis, M. G. *Chem. Mater.* **2009**, *21*, 1361. (c) Poudeu, P. F. P.; Gueguen, A.; Wu, C. I.; Hogan, T.; Kanatzidis, M. G. *Chem. Mater.* **2010**, *22*, 1046. (d) He, J. Q.; Sootsman, J. R.; Girard, S. N.; Zheng, J. C.; Wen, J. G.; Zhu, Y. M.; Kanatzidis, M. G.; Dravid, V. P. *J. Am. Chem. Soc.* **2010**, *132*, 8669.

(11) Biswas, K.; He, J. Q.; Zhang, Q. C.; Wang, G. Y.; Uher, C.; Dravid, V. P.; Kanatzidis, M. G. *Nat. Chem.* **2011**, *3*, 160.

(12) Androulakis, J.; Todorov, I.; Chung, D.-Y.; Ballikaya, S.; Wang, G. Y.; Uher, C.; Kanatzidis, M. G. *Phys. Rev. B* **2010**, *82*, 115209.

(13) Androulakis, J.; Todorov, I.; He, J. Q.; Chung, D.-Y.; Dravid, V. P.; Kanatzids, M. G. *J. Am. Chem. Soc.* **2011**, *133*, 10920.

(14) Androulakis, J.; Yeseul, L.; Todorov, I.; Chung, D.-Y.; Kanatzids, M. G. *Phys. Rev. B* **2011**, *83*, 195209.

(15) Wang, H.; Pei, Y. Z.; Lalonde, A. D.; Snyder, G. J. *Adv. Mater.* **2011**, *23*, 1366.

(16) Johnsen, S.; He, J. Q.; Androulakis, J.; Dravid, V. P.; Todorov, I.; Chung, D.-Y.; Kanatzidis, M. G. *J. Am. Chem. Soc.* **2011**, *133*, 3460.

(17) Maltsev, Y. V.; Nensberg, E. D.; Petrov, A. V.; Semiletov, S. A.; Ukhanov, Y. I. *Phys. Solid State* **1967**, *8*, 1713.

(18) Wright, D. A. *Metall. Rev.* **1970**, *15*, 147.

(19) Wood, C. *Rep. Prog. Phys.* **1988**, *51*, 459.

(20) Popovich, N. S. *Czech. J. Phys.* **2005**, *55*, 739.

(21) Sootsman, J. R.; Pcionek, R. J.; Kong, H. J.; Uher, C.; Kanatzidis, M. G. *Chem. Mater.* **2006**, *18*, 4993.

(22) He, J. Q.; Sootsman, J. R.; Girard, S. N.; Zheng, J. C.; Wen, J. G.; Zhu, Y. M.; Kanatzidis, M. G.; Dravid, V. P. *J. Am. Chem. Soc.* **2010**, *132*, 8669.

(23) Zhao, L.-D.; Zhang, B. P.; Li, J.-F.; Zhou, M.; Liu, W.-S.; Liu, J. *J. Alloys Compd.* **2008**, *455*, 259.

(24) Zhao, X. Y.; Shi, X.; Chen, L. D.; Zhang, W. Q.; Bai, S. Q.; Pei, Y. Z.; Li, X. Y.; Goto, T. *J. Appl. Phys.* **2006**, *89*, 092121.

(25) (a) Sootsman, J. R.; Kong, H. J.; Uher, C.; D'Angelo, J. J.; Wu, C. T.; Hogan, T. P.; Caillat, T.; Kanatzidis, M. G. *Angew. Chem., Int. Ed.* **2008**, *47*, 8618. (b) He, J. Q.; Sootsman, J. R.; Xu, L. Q.; Girard, S. N.; Zheng, J. C.; Kanatzidis, M. G.; Dravid, V. P. *J. Am. Chem. Soc.* **2011**, *133*, 8786–8789.

(26) Li, H.; Tang, X. F.; Su, X. L.; Zhang, Q. J. *Appl. Phys. Lett.* **2008**, *92*, 202114.

(27) Kim, W.; Zide, J.; Gossard, A.; Klenov, D.; Stemmer, S.; Shakouri, A.; Majumdar, A. *Phys. Rev. Lett.* **2006**, *96*, 045901.

(28) (a) Poudeu, P. F. P.; D'Angelo, J. J.; Kong, H.; Downey, A.; Short, J. L.; Pcionek, R.; Hogan, T. P.; Uher, C.; Kanatzidis, M. G. *J. Am. Chem. Soc.* **2006**, *128*, 14347. (b) Bilc, D.; Mahanti, S. D.; Quarez, E.; Hsu, K. F.; Pcionek, R.; Kanatzidis, M. G. *Phys. Rev. Lett.* **2004**, *93*, 146403.

(29) He, J. Q.; Steven, N. G.; Kanatzidis, M. G.; Vinayak, P. D. *Adv. Funct. Mater.* **2010**, *20*, 764.

(30) Garvin, P. F. *Neues Jahrb. Mineral., Abh.* **1973**, *118*, 235.

(31) Blachnik, R.; Igel, R. *Z. Naturforsch., B* **1974**, *29*, 625.

(32) Fitsul, V. I. *Heavily Doped Semiconductors*; Plenum Press: New York, 1969.

(33) Kumar, G. S.; Prasad, G.; Pohl, R. O. *J. Mater. Sci.* **1993**, *8*, 4261.

(34) Liu, W.-S.; Zhang, Q.; Lan, Y.; Chen, S.; Yan, X.; Zhang, Q.; Wang, H.; Wang, D.; Chen, G.; Ren, Z. F. *Adv. Energy Mater.* **2011**, *1*, 577.

(35) Zhao, L.-D.; Zhang, B. P.; Liu, W.-S.; Li, J.-F. *J. Appl. Phys.* **2009**, *105*, 023704.

(36) Zhou, M.; Li, J.-F.; Kita, T. *J. Am. Chem. Soc.* **2008**, *130*, 4527.

(37) Ravich, I. I.; Efimova, B. A.; Smirnov, I. A. *Semiconducting Lead Chalcogenides*; Plenum Press: New York, 1970.

(38) Hoang, K.; Mahanti, S. D.; Kanatzidis, M. G. *Phys. Rev. B* **2010**, *81*, 115106.

(39) Smirnov, I. A.; Moizhes, B. Y.; Nensberg, E. D. *Phys. Solid State* **1961**, *2*, 1793.

(40) Goldsmid, H. J. *Introduction to Thermoelectricity*; Springer Series in Materials Science; Springer: Heidelberg, 2010.

(41) Bozin, E.; Malliakas, C. D.; Souvatzis, P.; Proffen, T.; Spaldin, N. A.; Kanatzidis, M. G.; Billinge, S. J. L. *Science* **2010**, *330*, 1660.

(42) Liu, W.-S.; Zhang, B. P.; Li, J.-F.; Zhang, H. L.; Zhao, L.-D. *J. Appl. Phys.* **2007**, *102*, 103717.

(43) Toprak, S. M.; Stiewe, C.; Platzek, D.; Williams, S.; Bertini, L.; Muller, E.; Gatti, C.; Zhang, Y.; Rowe, M.; Muhammed, M. *Adv. Funct. Mater.* **2004**, *14*, 1189.

(44) Koh, Y. K.; Vineis, C. J.; Calawa, S. D.; Walsh, M. P.; Cahill, D. G. *Appl. Phys. Lett.* **2009**, *94*, 153101.